Synthesis, characterization and electrochemical performance of Al-substituted Li$_2$MnO$_3$

Loraine Torres-Castro [a], Jifi Shojan [a,b], Christian M. Julien [c], Ashfia Huq [d], Chetan Dhital [d], Mariappan Parans Paranthaman [e], Ram S. Katiyar [a,b], Ayyakkannu Manivannan [f,g,*]

[a] Department of Physics and The Chemical Physics Graduate Program, University of Puerto Rico, San Juan, PR 00931, USA
[b] Institute for Functional Nanomaterials, University of Puerto Rico, San Juan, PR 00931, USA
[c] Physicochimie des Electrolytes, Colloïdes et Sciences Analytiques, Université Pierre et Marie Curie-Paris-6 75005, Paris, France
[d] Chemical and Engineering Materials Division, Oak Ridge National Laboratory, Oak Ridge, TN 37831, USA
[e] Chemical Sciences Division, Oak Ridge National Laboratory, Oak Ridge, TN 37831, USA
[f] United States Department of Energy, National Energy Technology Laboratory, Morgantown, WV 26507, USA
[g] Mechanical and Aerospace Engineering, West Virginia University, Morgantown, WV 26507, USA

ARTICLE INFO

ABSTRACT

Li$_2$MnO$_3$ is known to be electrochemically inactive due to Mn in tetravalent oxidation state. Several compositions such as Li$_2$MnO$_3$, Li$_{1.5}$Al$_{0.17}$MnO$_3$, Li$_{1.0}$Al$_{0.33}$MnO$_3$ and Li$_{0.5}$Al$_{0.5}$MnO$_3$ were synthesized by a sol–gel Pechini method. All the samples were characterized with XRD, Raman, XPS, SEM, Tap density and BET analyzer. XRD patterns indicated the presence of monoclinic phase for pristine Li$_2$MnO$_3$ and mixed monoclinic/spinel phases (Li$_{2-x}$Mn$_{1-y}$Al$_{x+y}$O$_{3+z}$) for Al-substituted Li$_2$MnO$_3$ compounds. The Al substitution seems to occur both at Li and Mn sites, which could explain the presence of spinel phase. XPS analysis for Mn 2p orbital reveals a significant decrease in binding energy for Li$_{1.0}$Al$_{0.33}$MnO$_3$ and Li$_{0.5}$Al$_{0.5}$MnO$_3$ compounds. Cyclic voltammetry, charge/discharge cycles and electrochemical impedance spectroscopy were also performed. A discharge capacity of 24 mAh g^{-1} for Li$_2$MnO$_3$, 68 mAh g^{-1} for Li$_{1.5}$Al$_{0.17}$MnO$_3$, 58 mAh g^{-1} for Li$_{1.0}$Al$_{0.33}$MnO$_3$ and 74 mAh g^{-1} for Li$_{0.5}$Al$_{0.5}$MnO$_3$ were obtained. Aluminum substitutions increased the formation of spinel phase which is responsible for cycling.

Published by Elsevier B.V.

1. Introduction

Lithium ion batteries have gained increased popularity among the scientific community due to their high energy density and long cycle life. Although, lithium-ion batteries are widely commercialized and are more popular for portable units such as cell phones and laptops, there are still limitations and needs improvement [1]. Many efforts have been made to search for new cathode materials that could potentially satisfy the market for high demand portable electronic devices and electric vehicle technology [2–4]. Among the cathode materials investigated, lithium manganese oxides have been exploited due to the abundance of Mn in earth, low toxicity and safety [5]. In this family of oxides, LiMnO$_2$ and LiMn$_2$O$_4$

showed promising electrochemical properties, such as high discharge capacity and high operating voltage, respectively. However, these materials suffer from serious structural changes after certain number of cycles due to the presence of Mn^{3+} ion, which is known to be a Jahn–Teller active ion [6]. Side reactions such as 2Mn^{3+} → Mn^{4+} + Mn^{2+}, also lead to battery failure upon cycling, as Mn^{2+} is known to be soluble in non-aqueous electrolytes. Li$_2$MnO$_3$ belongs to the same family of oxide materials having a monoclinic structure with C2/m space group symmetry. The A$_2$BO$_3$ rock-salt type configuration possesses a layered arrangement that can be represented as Li [Li$_{1/3}$Mn$_{2/3}$] O$_2$. In other words, in Li$_2$MnO$_3$, 1/3 of the Mn-ions in the transition-metal layer are replaced with Li ions. Layers of lithium ions and alternating layers of manganese ions are separated from one another by layers of cubic-close packed oxygen planes, thus resembling the ideal layered structure of LiCoO$_2$ [7]. The existence of lithium in the transition metal layer provides a high theoretical capacity (460 mAh g^{-1}), which makes it a promising cathode material for Li-ion batteries. Li$_2$MnO$_3$ has been widely studied due to its electrochemical activity in the high voltage region, i.e. >4.5 V vs. Li^0/Li$^+$. Its electrochemical behavior has

* Corresponding author at: United States Department of Energy/National Energy Technology Laboratory, 3610 Collins Ferry Rd., P.O. Box 880 Morgantown, WV 26507-0880, USA. Tel.: +1 304 285 2078.
E-mail addresses: manivana@netl.doe.gov, amanivan@wvu.edu (A. Manivannan).

also been explored by a chemical delithiation process; however this compound has not been well characterized for lithium substitution [8].

The drawback of Li_2MnO_3 is the presence of Mn in +4 oxidation state, which makes the material electrochemically inactive. Despite, it can be made electrochemically active by extracting lithium and oxygen simultaneously from the structure by chemical or electrochemical means [8]. The activation of Li_2MnO_3 due to extraction of lithium along with oxygen by chemical treatments with HNO_3 and H_2SO_4 has also been reported [9]. However, during the electrochemical reaction a phase transformation is observed where the new spinel structure is formed [9]. In addition, electrochemical activation has been achieved after exposing the electrode to potentials higher than 4.5 V vs. Li^0/Li^+, which causes the partial removal of lithium and oxygen from the structure [10]. In both cases, the activation process leads to the rearrangement of ions resulting in vacancies in the host structure, which allow the reversible intercalation of lithium.

Recently, researchers have been studying the effects of partially substituted manganese ions with other transition metals such as ruthenium, where a reversible capacity of $210 \, mAh \, g^{-1}$ was obtained by 40% substitution of manganese [11]. Mori et al. also investigated the effect of Ru doping in Li_2MnO_3, obtaining a discharge capacity of $192 \, mAh \, g^{-1}$ for 60% substitution of manganese, while at 80% the capacity was $\sim 180 \, mAh \, g^{-1}$. Ruthenium substitution studies demonstrated a noticeable improvement on the electrochemical performance of the cathode material due to the ability of ruthenium to be oxidized [12]. Kim et al. studied the effect of Al, Cr, Zn and Fe doping in the Mn-site of Li_2MnO_3. They observed that doping small amounts of these transition metals in the structure improved the electrochemical performance dramatically for the first discharge capacity ($200–240 \, mAh \, g^{-1}$) [13]. A different approach reported by Amalraj et al. was the synthesis of nanosized Li_2MnO_3 to decrease the particle size and increase the surface area, which lead to an increase in capacity of 75% ($207 \, mAh \, g^{-1}$) compared to the micron sized Li_2MnO_3 ($28 \, mAh \, g^{-1}$) [14]. The same research group performed a study about the relationship between cycling temperature and electrochemical behavior of the electrodes. They established that higher temperatures enhance the electrochemical performance as well as the cycle stability. In order to reduce the initial irreversible loss that Li_2MnO_3 is known for, Wang et al. coated the surface of the pristine material with $FePO_4$, where an improved capacity and cycle stability was achieved [15]. Instead of substituting Mn site, Dong et al. studied Li site substitution with sodium to partially remove lithium. An improved capacity of $216 \, mAh \, g^{-1}$ for the initial cycle and $109 \, mAh \, g^{-1}$ for the 100th cycle was reported [16].

In the present study, we investigated the electrochemical and structural properties of Li_2MnO_3 at room temperature by partially substituting Li with Al using the sol–gel Pechini method. The substitution in $Li_{1.5}Al_{0.17}MnO_3$, $Li_{1.0}Al_{0.33}MnO_3$ and $Li_{0.5}Al_{0.5}MnO_3$ compounds is based on the charge balance where Al has a +3 oxidation state compared to Li with +1 oxidation state. The effect of the Al ion substitution at the Mn and Li sites indicated improved structural and electrochemical behavior compared to the pristine Li_2MnO_3.

2. Experimental

Li_2MnO_3, $Li_{1.5}Al_{0.17}MnO_3$, $Li_{1.0}Al_{0.33}MnO_3$ and $Li_{0.5}Al_{0.5}MnO_3$ were synthesized using the sol–gel Pechini method [17]. For the individual compounds, synthesis was carried out using lithium nitrate [$LiNO_3$ >98%; Luka], manganese nitrate [$Mn(NO_3)_2$ 50% w/w aq. soln.; Alfa Aesar], aluminum nitrate nonahydrate

[$Al(NO_3)_3 \cdot 9H_2O$ 98–102%; Alfa Aesar], ethylene glycol [$C_2H_6O_2$ >99%; Alfa Aesar] (EG) and citric acid [$H_3C_6H_5O_7$ >99.5%; Alfa Aesar] (CA) as the starting precursors materials. The molar ratio of M:EG:CA used was 1:1.2:1.2, where M is the sum of all metal ions. Stoichiometric ratios of the metals corresponding to each composition were measured and dissolved in deionized water along with CA, which behaves as a chelating reagent. The solution was heated at 80 °C for 10 min before adding ethylene glycol to serve as the complex cross-linking reagent. As the water concentration decreased, the solution became a gel-like appearance. The beaker was transferred into a heating mantle kept at a temperature of 130 °C, until all the NO_x gases released to form a 3D-polymeric structure. The resulting dark grey color powder was placed in an oven at 130 °C for 24 h to complete the drying process. The final dried powder was annealed at 750 °C for 8 h in air to form the final compound which was bright orange in color.

The structural phase identification of the materials and the presence of any crystalline impurities in the compounds were studied with PANalytical X'Pert Powder diffractometer (XRD) using a CuK_α radiation ($\lambda = 1.54056 \, Å$). XRD spectra were acquired at 45 kV and 40 mA for a 2θ ranging from 10 to 90°. Time of flight (TOF) neutron diffraction measurements were performed at POWGEN powder diffractometer at the Spallation Neutron Source (SNS), Oak Ridge National Laboratory. The data were collected with a central wavelength of 1.066 Å at both 300 K and 10 K. This facility covers a d-spacing range of 0.276–4.606 Å. Raman scattering (RS) spectra were recorded using a T6400 spectrometer equipped with a triple grating monochromator and a Coherent Innova 90C Ar laser at 514.5 nm. The morphology of the samples was analyzed with a scanning electron microscope (SEM) conducted with JEOL 7600 FE-SEM interfaced with a Thermo-Electron S7 X-ray Microanalysis system. System was calibrated using $CuK_\alpha = 8.041 \, keV$. The specific surface area was measured with the Brunauer, Emmett, and Teller (BET) method using an ASAP 2020, Micromeritics. Tap density analysis was performed with an Autotap Quantachrome instrument.

X-ray photoelectron spectroscopy (XPS) spectra were obtained utilizing a Physical Electronics (PE) SAM-590 UHV system equipped with a PE spherical capacitor type analyzer with an Omni Focus III Lens and a PE 04-303 Ar-ion Gun. Binding energies (BEs) were referenced to adventitious carbon at 284.8 eV [18].

The electrochemical behavior of the as-synthesized materials was examined in a two-electrode CR2032-type coin cell configuration using liquid electrolytes consisting of $1 \, mol \, L^{-1} \, LiPF_6$ dissolved in 1:2 (v/v) mixture of ethylene carbonate (EC) and dimethyl carbonate (DMC). The working electrode was fabricated by mixing 80 wt.% of the active material, 10 wt.% of polyvinylidene fluoride binder (PVDF, Alfa Aesar) and 10 wt.% of carbon black (Alfa Aesar) [19]. The slurry was prepared using 1-methyl 2-pyrolidone as the solvent and was coated onto Al foil substrates to form a homogeneous electrode. Li metal foil was used as the counter electrode and Celgard 2400 was used as a separator between anode and cathode. The coin cell was assembled inside the Ar-filled glove box (MBraun, O_2 and H_2O < 1 ppm).

The electrochemical analysis of the coin cells was investigated with cyclic voltammetry (CV), charge/discharge process (C/D) and electrochemical impedance spectroscopy (EIS). Cyclic voltammetry was performed on the coin cells at a scan speed of $0.1 \, mV \, s^{-1}$ and a potential range of 2.0–4.8 V with a Solartron Analytical 1470E Cell Test station. The cells were tested using a constant current method (C/D) of 0.05 C ($10 \, mA \, g^{-1}$) with a potential window ranging from 2.8 to 4.8 V on an Arbin 60 channels battery tester. The impedance was measured using the ac voltage of 5 mV over a frequency range of 100 kHz to 10 mHz using a Solartron Analytical 1252A Frequency Response Analyzer.

Table 1

Lattice parameters of Li_2MnO_3, $Li_{1.5}Al_{0.17}MnO_3$, $Li_{1.0}Al_{0.33}MnO_3$ and $Li_{0.5}Al_{0.5}MnO_3$ based on the monoclinic structure. Lattice parameters for the Al substituted Li_2MnO_3 phases based on the spinel structure is reported in Table 2.

Composition	a (Å)	b (Å)	c (Å)	β (°)	V (A³)	XS (nm)
Li_2MnO_3	4.9086	8.4742	4.9988	108.95	196.66	49.6 (2)
$Li_{1.5}Al_{0.17}MnO_3$	4.9811	8.5289	5.0034	108.95	201.00	21.2 (2)
$Li_{1.0}Al_{0.33}MnO_3$	5.0356	8.5367	5.0231	110.90	201.70	31.2 (1)
$Li_{0.5}Al_{0.5}MnO_3$	5.0442	8.5383	5.9625	111.30	239.30	47.6 (1)
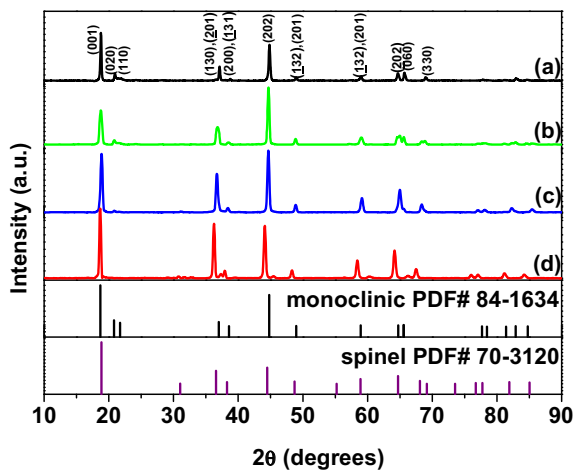
Fig. 1. X-ray powder diffraction patterns of (a) Li_2MnO_3, (b) $Li_{1.5}Al_{0.17}MnO_3$, (c) $Li_{1.0}Al_{0.33}MnO_3$ and (d) $Li_{0.5}Al_{0.5}MnO_3$ compounds.

Table 2

Lattice parameters of $Li_{1.5}Al_{0.17}MnO_3$, $Li_{1.0}Al_{0.33}MnO_3$ and $Li_{0.5}Al_{0.5}MnO_3$ based on the spinel (cubic) structure.

Composition	a (Å)	$\alpha = \beta = \gamma$	V (A³)
Spinel $LiMn_2O_4$ (cubic)*	8.2210	90	555.6
$Li_{1.5}Al_{0.17}MnO_3$	8.9330	90	712.8
$Li_{1.0}Al_{0.33}MnO_3$	8.5182	90	618.1
$Li_{0.5}Al_{0.5}MnO_3$	8.3495	90	582.1

* Fitted using the PDF# 70-3120.

3. Results and discussion

3.1. X-ray diffraction:

Powder X-ray diffraction patterns for Li_2MnO_3, $Li_{1.5}Al_{0.17}MnO_3$, $Li_{1.0}Al_{0.33}MnO_3$ and $Li_{0.5}Al_{0.5}MnO_3$ compounds synthesized by a sol–gel Pechini method are shown in Fig. 1. The pristine Li_2MnO_3 diffraction pattern displayed no impurity peaks as demonstrated in Fig. 1a, matching with the PDF# 84-1634. This confirms the presence of a single phase for Li_2MnO_3 with lattice parameters in agreement with the literature values [14,20–22]. The XRD pattern for $Li_{1.5}Al_{0.17}MnO_3$ (Fig. 1b) showed all the diffraction peaks similar to Li_2MnO_3. However, some of the peaks were split at the top, which represents a spinel phase in the structure. Fig. 1c presents the XRD profile for $Li_{1.0}Al_{0.33}MnO_3$ compound, in which a spinel phase formation is revealed. Fig. 1d shows the XRD pattern for $Li_{0.5}Al_{0.5}MnO_3$ compound where the intensities of the characteristic peaks ($2\theta = 20–23°$) of C2/m group symmetry are weak. These characteristic peaks are due to the presence of lithium in the transition metal layers and, identified in the lattice with the Miller indices (hkl) of (0,2,0) and (1,1,0), in which only lithium and oxygen are present in the plane. The intensity of this peak seems to decrease as the amount of aluminum substitution is increased, which could be due to the simultaneous substitution of aluminum into the manganese and lithium sites or loss of lithium during synthesis. The diffraction peaks were fitted based on the monoclinic Li_2MnO_3 for
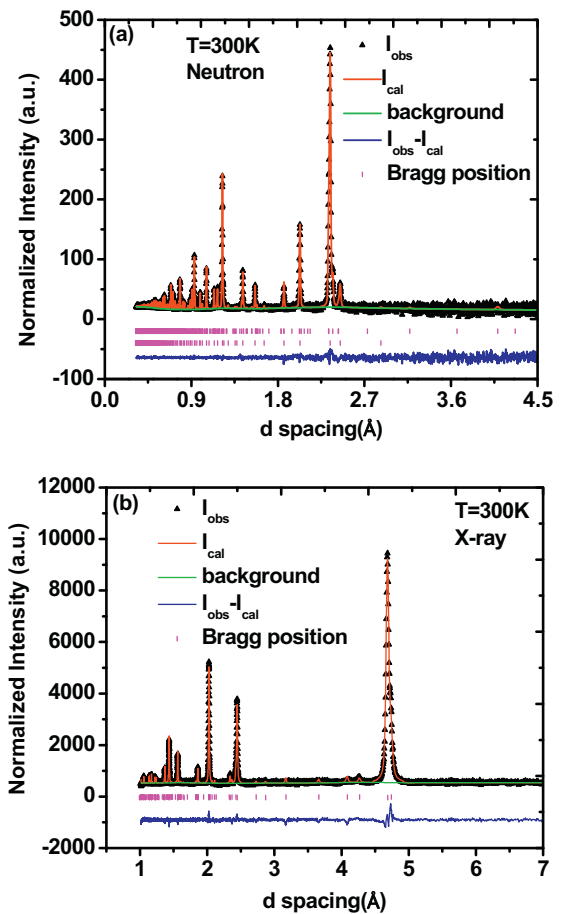
Fig. 2. Neutron diffraction (a) phase I: monoclinic (b) phase II: spinel.

which a Rietveld refinement was performed to obtain the lattice parameters listed in Table 1.

All the compositions contain a spinel phase in addition to the monoclinic phase due to the substitution of aluminum ions. Table 2 shows the lattice parameters for the Al-substituted Li_2MnO_3 compounds based on the fitting for a spinel phase. As we increase the amount of aluminum substitution, the 'a' lattice parameter approaches the value for the spinel phase, demonstrating the influence of aluminum ions towards the formation of a spinel phase. On the other hand, when observing the lattice parameters based on fitting for a monoclinic phase, it seems that the compounds with the lowest substitution of aluminum have similar lattice parameters values as the monoclinic phase. Based on the observations made by XRD analysis we conclude that spinel phase will be more prominent as we increase the amount of Al substitution.

3.2. Neutron diffraction:

To further understand the structure, neutron diffraction measurement was performed on one of the compositions ($Li_{1.0}Al_{0.33}MnO_3$). A combined X-ray/neutron Rietveld refinement

Table 3
Time of flight (TOF) neutron diffraction measurement refinements for the monoclinic phase.

Phase I
Monoclinic Li_2MnO_3
$a = 4.9278(6)$ $b = 8.5351(9)$ $c = 5.02012(35)$
$\alpha = 90$ $\beta = 109.201(8)$ $\gamma = 90$
Space group: C2/m
Composition: Li2(0)Mn1(0)O3(0)
Wt. fraction = 0.19 ± 0.004

Name	X	esd	Y	esd	Z	esd	Uiso	esd	Occupancy	esd
Li1	0.000	0.000	0.500	0.000	0.000	0.000	0.006	0.000	1.000	0.000
Al1	0.000	0.000	0.500	0.000	0.000	0.000	0.005	0.000	0.000	0.000
Mn1	0.000	0.000	0.500	0.000	0.000	0.000	0.005	0.000	0.000	0.000
Li2	0.000	0.000	0.000	0.000	0.500	0.000	0.006	0.000	1.000	0.000
Al2	0.000	0.000	0.000	0.000	0.500	0.000	0.005	0.000	0.000	0.000
Mn2	0.000	0.000	0.000	0.000	0.500	0.000	0.005	0.000	0.000	0.000
Li3	0.000	0.000	0.681	0.000	0.500	0.000	0.005	0.000	1.000	0.000
Al3	0.000	0.000	0.681	0.000	0.500	0.000	0.005	0.000	0.000	0.000
Mn3	0.000	0.000	0.681	0.000	0.500	0.000	0.005	0.000	0.000	0.000
Mn4	0.000	0.000	0.170	0.000	0.000	0.000	0.001	0.000	1.000	0.000
O1	0.271	0.000	0.000	0.000	0.213	0.000	0.027	0.000	1.000	0.000
O2	0.232	0.000	0.335	0.000	0.227	0.000	0.007	0.000	1.000	0.000
Li1A	0.000	0.000	0.500	0.000	0.000	0.000	0.015	0.000	0.000	0.000
Li2A	0.000	0.000	0.000	0.000	0.500	0.000	0.015	0.000	0.200	0.000
Li3A	0.000	0.000	0.681	0.000	0.500	0.000	0.015	0.000	0.300	0.000
Li4A	0.000	0.000	0.168	0.000	0.000	0.000	0.015	0.000	0.000	0.000

Table 4
Time of flight (TOF) neutron diffraction measurement refinements for the spinel phase.

Phase II (Spinel)
$Li_{1.06}Al_{0.44}Mn_{1.5}O_4$
$a = 8.11719(5)$
$\alpha = 90$ $\beta = 90$ $\gamma = 90$
Space group: Fd-3m
Composition: $\{Li_{0.982(5)Al0.018(5)}\}\{Li_{0.078(8)}Al_{0.422(8)}Mn_{1.5(8)}\}O_4$
Wt. fraction = 0.81 ± 0.002

Name	X	esd	Y	esd	Z	esd	Uiso	esd	Occupancy	esd
Li1	0.125	0.000	0.125	0.000	0.125	0.000	0.008	0.001	0.982	0.005
AL1	0.125	0.000	0.125	0.000	0.125	0.000	0.008	0.001	0.018	0.005
Mn2	0.500	0.000	0.500	0.000	0.500	0.000	0.009	0.000	0.694	0.004
AL2	0.500	0.000	0.500	0.000	0.500	0.000	0.009	0.000	0.211	0.004
Li2	0.500	0.000	0.500	0.000	0.500	0.000	0.009	0.000	0.039	0.004
Mn2a	0.500	0.000	0.500	0.000	0.500	0.000	0.009	0.000	0.056	0.004
O1	0.263	0.000	0.263	0.000	0.263	0.000	0.009	0.001	1.000	0.000

was performed with a GSAS software. The results of the refinements are presented in Table 3 and Table 4. The refinement presented in Fig. 2, shows that the sample is a mixture of two phases: Monoclinic (C2/m) Li_2MnO_3, and Spinel $(Li,Al)(Mn,Al)_2O_4$. We tested mainly four possibilities assigning aluminum to (a) lithium site in the monoclinic phase, (b) manganese site in the monoclinic phase, (c) lithium site in the spinel phase and (d) manganese site in the spinel phase. Out of these four possibilities, the assignment of Al to Mn site in the spinel phase best describes our data.

3.3. Raman scattering:

In order to fully understand the effect of Al substitution on the structure of Li_2MnO_3, Raman spectra were obtained (Fig. 3). The Raman spectra for the pristine Li_2MnO_3 cathode material, shown in Fig. 3a, exhibits nine resolved peaks at 248, 309, 323, 368, 414, 431, 487, 559 and 607 cm^{-1}, which are in good agreement with those reported by Amalraj et al. [23]. According to their theoretical calculations, the monoclinic Li_2MnO_3 oxide with C_{2h}^3 spectroscopic symmetry is predicted to show 10 Raman-active modes with $4A_g + 6B_g$ species. The peaks at low wavenumbers are linked to the vibration of the LiO_6 octahedral and to the O–Mn–O bending modes (B_g modes), while high wavenumber peaks are related to the stretching modes of the Mn–O bonds (A_g modes) [24–26]. These later vibrations are mostly due to the O–O motions since Mn ions located at the octahedron center do not vibrate in the Raman A_g modes. The Raman spectra of $Li_{1.5}Al_{0.17}MnO_3$ are almost identical to that of the pristine sample, with a slight shift that is within the acceptable range. An additional peak occurs at 654 cm^{-1} which is attributed to the presence of Al–O bonds. The Raman spectra of $Li_{1.0}Al_{0.33}MnO_3$ and $Li_{0.5}Al_{0.5}MnO_3$ (Fig. 3b) display a different profile that indicates different structural arrangement of atoms in the lattice. The spectrum contains seven bands at 350, 394, 431, 479, 540, 605, and 646 cm^{-1} for $Li_{1.0}Al_{0.33}MnO_3$ and nine bands at 278, 328, 360, 402, 454, 486, 547, 597 and 630 cm^{-1} for $Li_{0.5}Al_{0.5}MnO_3$. The substitution of Li with Al induces the presence of an additional phase with a spinel structure.

Preudhome and Tarte [27] claimed that if there are two different octahedra in a structure, with different vibrational frequencies, their vibrational interaction is going to be weak resulting in individual contributions to the spectrum at their respective distinctive frequencies. It is the case for $Li_{1.0}Al_{0.33}MnO_3$ and $Li_{0.5}Al_{0.5}MnO_3$ framework, which contains MnO_6 and AlO_6 octahedra. Following this thought, the high wavenumber peak of $Li_{1.0}Al_{0.33}MnO_3$ and $Li_{0.5}Al_{0.5}MnO_3$ located at 646 cm^{-1} and 630 cm^{-1} respectively, is
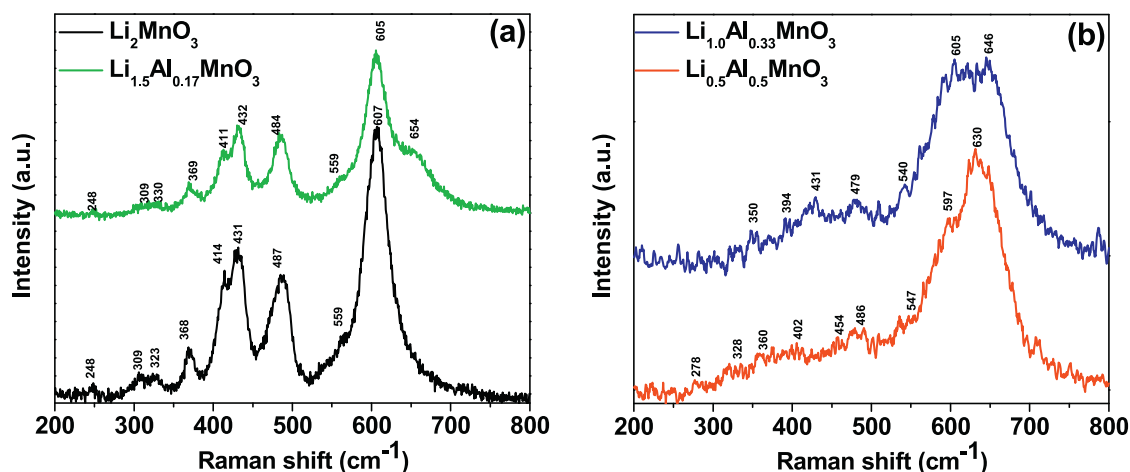
Fig. 3. Raman scattering spectra of (a) Li_2MnO_3, $Li_{1.5}Al_{0.17}MnO_3$ and (b) $Li_{1.0}Al_{0.33}MnO_3$, $Li_{0.5}Al_{0.5}MnO_3$.

due to the stretching modes of the Al–O bonds (A_{1g} mode), while the low wavenumber peaks at 540, 479, 431, 394 and 350 cm^{-1} for $Li_{1.0}Al_{0.33}MnO_3$ and 547, 486, 454, 402, 360, 328 and 278 cm^{-1} for $Li_{0.5}Al_{0.5}MnO_3$ have the T_{2g} character for the (Mn, Al)–O bond vibrations.

3.4. SEM and EDX:

The powder morphology of the synthesized samples was analyzed with SEM. It is important to determine the particle size of the materials because it is known that electrochemical performance of an electrode is strongly dependent on the particle size. For small particle size, the specific surface area is higher, allowing easy kinetics for insertion/extraction of Li$^+$ ions leading to high energy density. The SEM images are shown in Fig. 4, where the materials synthesized with the sol–gel Pechini method resulted in the formation of agglomerates. It

can be observed that the particle size of the pristine Li_2MnO_3 and Al-substituted compounds are similar and are displaying high agglomeration of the primary particles. EDX analysis performed over the agglomerated area and its surrounding indicates the existence of the respective elements in the compounds.

3.5. BET analysis

The BET surface area was measured for the samples using nitrogen adsorption–desorption isotherms. The surface area for Li_2MnO_3, $Li_{1.5}Al_{0.17}MnO_3$ (25% Al-substitution), $Li_{1.0}Al_{0.33}MnO_3$ (50% Al-substitution) and $Li_{0.5}Al_{0.5}MnO_3$ (75% Al-substitution) were determined to be 2.05, 13.36, 19.92 and 10.87 m^2 g^{-1} respectively as shown in Fig. 5. Amalraj et al. reported a surface area for the pristine Li_2MnO_3 synthesized by a solid-state route to be 0.86 m^2 g^{-1} [14]. Therefore, the sol–gel Pechini method doubles

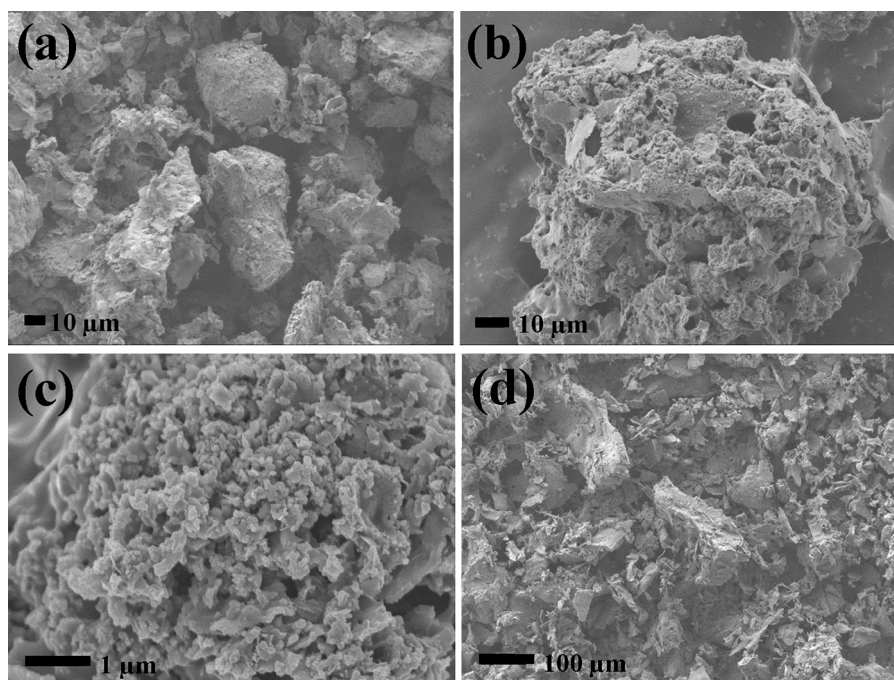**Fig. 4.** Scanning electron microscopy images of (a) Li_2MnO_3, (b) $Li_{1.5}Al_{0.17}MnO_3$, (c) $Li_{1.0}Al_{0.33}MnO_3$ and (d) $Li_{0.5}Al_{0.5}MnO_3$.

Fig. 5. BET surface area and tap density analysis of Li_2MnO_3 and Al-substituted compounds.

Table 5
XPS binding energies for Mn 2p orbital.

Composition	B.E. (eV) Mn 2p$_{1/2}$	B.E. (eV) Mn 2p$_{3/2}$	ΔB.E. Mn 2p (eV)
Li_2MnO_3	654.10	642.30	11.80
$Li_{1.5}Al_{0.17}MnO_3$	655.10	643.40	11.70
$Li_{1.0}Al_{0.33}MnO_3$	653.50	641.90	11.60
$Li_{0.5}Al_{0.5}MnO_3$	653.85	642.25	11.60

(641.90 eV and 642.25 eV, respectively) compared to the pristine Li_2MnO_3 (642.30 eV). The change to a lower binding energy is an indication of a reduction in the valence state of manganese ($Mn^{<4+}$) which could enable this material to cycle with an enhanced capacity. In the case of $Li_{1.5}Al_{0.17}MnO_3$, the peaks are slightly shifted to higher binding energies, indicating no change in the valence state of manganese. The lower binding energy obtained from XPS results for $Li_{1.0}Al_{0.33}MnO_3$ and $Li_{0.5}Al_{0.5}MnO_3$ compounds suggest we could expect an improvement in the electrochemical performance.

3.7. Electrochemical characterization

The electrochemical performance of the cathode materials was investigated with cyclic voltammetry (CV) to observe the redox processes. The potential window used was 2.0–4.8 V at a scanning rate of 0.1 mV s^{-1}. Three consecutive CV measurements were performed to understand the redox reaction before and after charge/discharge cycles. The first CV for Li_2MnO_3, shown in Fig. 7(a), presents the distinctive anodic and cathodic peaks for this material at 3.33 and 2.67 V, respectively. A broader oxidation peak is observed around 4.07 V, which is the evidence for phase transition in the structure from layer to spinel as reported in the literature [28]. After each cyclic voltammetry, the current intensity at the anodic peak was decreasing and the voltage shifted to higher potential values. On the contrary, the cathodic peak current intensity was increasing and moving to lower potentials, which reveal a separation between the anodic and cathodic peaks, indicative of an irreversible process. The CV behavior for the Al-substituted compounds is similar to spinel phase materials as well as monoclinic Li_2MnO_3, which was expected since spinel phase was observed in both XRD and RAMAN analysis. The oxidation and reduction peaks for the spinel phase materials correspond to the process associated with Mn^{4+}/Mn^{3+} but in our case the oxidation peaks corresponds to $Mn^{4+}/Mn^{3.5-3.9+}$ as shown by XPS analysis. In addition, pure spinel phase presents a lower separation of peak potentials compared to our compounds, which indicates the combination of two phases (monoclinic along with spinel) for the Al-substituted Li_2MnO_3. Cyclic voltammogram of $Li_{1.5}Al_{0.17}MnO_3$ showed a similar behavior to the pristine sample (Fig. 7b). The anodic peak at ~4.68 V is due to the partial extraction of lithium and oxygen ions from the structure. In the case of $Li_{1.0}Al_{0.33}MnO_3$, (Fig. 7c), two anodic peaks at 3.29 V and 4.17 V were observed. The current intensity of the first anodic peak decreases after each CV, while the voltage remains fairly similar. The second cathodic peak exhibited a shift to lower potential values with a slight increase in current after each cycle indicating the irreversible process during the electrochemical performance. Similarly, the first CV for $Li_{0.5}Al_{0.5}MnO_3$ (Fig. 7d) depicts well-defined anodic and cathodic peaks. The intensities of the oxidation and reduction peaks are higher and sharper than pristine Li_2MnO_3. The second CV exhibited a reduction in the voltage for the first anodic peak from 3.15 V to 3.07 V, while the current increased to 0.51 mA from 0.44 mA. In addition, the second anodic peak at 4.28 V confirms the presence of spinel phase in the structure, as observed in XRD and Raman. In the case of the peak around 2.61 V, a small change in voltage and current is observed after the first CV.
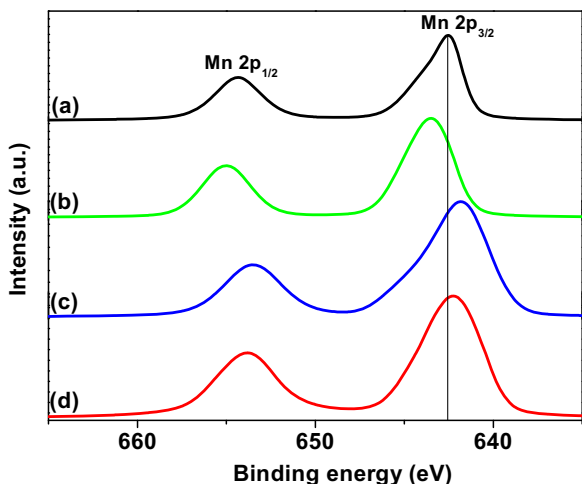
the surface area of Li_2MnO_3. In addition, the BET surface area for Al-substituted samples is significantly higher compared to the pristine Li_2MnO_3. Tap density analysis was performed for the compounds to complement the BET measurements since high surface area is inversely proportional to the packing density. $Li_{0.5}Al_{0.5}MnO_3$ exhibits a higher tap density and a smaller surface area among the Al-substituted compounds. The combination of both properties suggests that this compound will exhibit a higher energy density and a better cycle stability.

3.6. XPS

As mentioned before, the main objective of this work is to reduce the Mn valence state and investigate the electrochemical properties for improved cycling capacity. In order to understand the effects of these Al substitutions on the valence state of Mn, XPS spectra of the materials were performed. The XPS results presented in Fig. 6 indicate that Mn 2p spectra exhibited two major peaks due to the spin-orbit splitting for all compositions. The Mn 2p$_{1/2}$ and Mn 2p$_{3/2}$ binding energy values for the pristine Li_2MnO_3 are 654.10 eV and 642.30 eV, respectively, with a binding energy splitting of 11.8 eV. The XPS data for Mn 2p orbital for the Al-substituted compounds is presented in Table 5. The Mn 2p$_{3/2}$ peak for $Li_{1.0}Al_{0.33}MnO_3$ and $Li_{0.5}Al_{0.5}MnO_3$ is significantly shifted to a lower binding energy

Fig. 6. XPS spectra of (a) Li_2MnO_3, (b) $Li_{1.5}Al_{0.17}MnO_3$, (c) $Li_{1.0}Al_{0.33}MnO_3$ and (d) $Li_{0.5}Al_{0.5}MnO_3$.
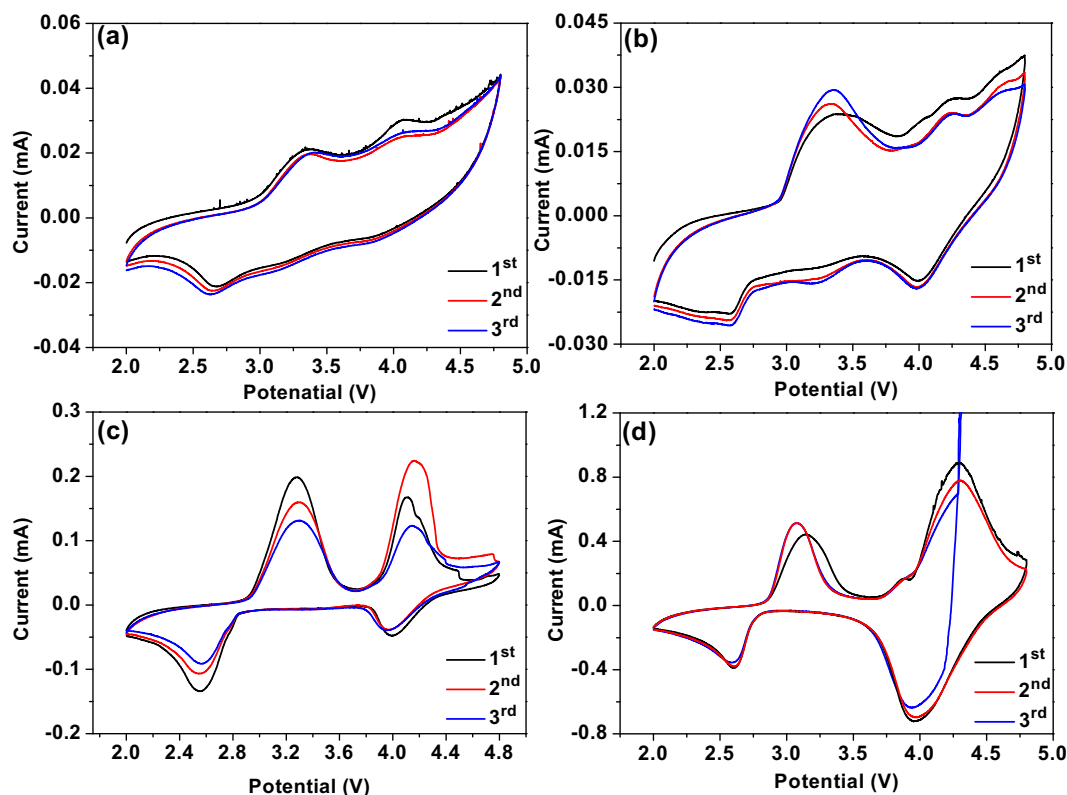
Fig. 7. Cyclic voltammograms of (a) Li_2MnO_3, (b) $Li_{1.5}Al_{0.17}MnO_3$, (c) $Li_{1.0}Al_{0.33}MnO_3$ and (d) $Li_{0.5}Al_{0.5}MnO_3$ in the voltage range of 2.0–4.8 V with a scan rate of 0.1 mV s^{-1}.

Table 6
Initial electrochemical performance.

Composition	1st charge capacity (mAh g^{-1})	1st discharge capacity (mAh g^{-1})	Coulombic efficiency (%) 1st cycle	Coulombic efficiency (%) 50th cycle
Li_2MnO_3	32	12	38%	90%
$Li_{1.5}Al_{0.17}MnO_3$	109	68	62%	96%
$Li_{1.0}Al_{0.33}MnO_3$	80	58	73%	99%
$Li_{0.5}Al_{0.5}MnO_3$	91	74	81%	99%

However, the current intensity and peak potential remain the same for the second and third CV scans.

The charge–discharge curves for pristine and Al-substituted Li_2MnO_3 are shown in Fig. 8. The current density used was 10 mA g^{-1} for a potential window of 2.8–4.8 V. Table 6 presents the first charge and discharge capacity of the compounds as well as the coulombic efficiency of the 1st and 50th cycle. First galvanostatic charge/discharge profile for Li_2MnO_3 shows a plateau at 4.5 V (Fig. 8a) that is related to lithium and oxygen extraction from the structure [29]. The specific capacity after charging was calculated to be 32 mA g^{-1}, with a corresponding discharge capacity of 12 mAh g^{-1}. The coulombic efficiency of the first cycle for pristine Li_2MnO_3 was 38% but it improved for consecutive cycles. At 50th cycle, the capacity was approximately 24 mAh g^{-1} with an efficiency of 90%. These results were expected since monoclinic phase compounds are known for its lack of electrochemical activities during redox process. Fig. 8b exhibits the charge/discharge profile of $Li_{1.5}Al_{0.17}MnO_3$ which displays a similar electrochemical behavior as Li_2MnO_3, showing higher first cycle discharge capacity of 68 mAh g^{-1} with an efficiency of 62%. After 50 cycles the capacity was around 58–55 mAh g^{-1} and continued to decrease after each cycle. A plateau at ~4.65 V is also observed for this compound, which refers to the extraction of lithium and oxygen from the host structure. $Li_{1.0}Al_{0.33}MnO_3$ showed an initial discharge capacity of 58 mAh g^{-1}, however, this compound demonstrated the best cycle

stability with a discharge capacity in the range of 60–62 mAh g^{-1} (Fig. 8c) and coulombic efficiency of ~99%. Charge–discharge curves for $Li_{0.5}Al_{0.5}MnO_3$ are shown in Fig. 8d and the initial discharge capacity exhibited 81% efficiency (74 mAh g^{-1}) compared to pristine Li_2MnO_3 (20 mAh g^{-1}). After 50 cycles, the capacity was ~70 mAh g^{-1} with a coulombic efficiency of 99%. The enhance electrochemical performance for the Al-substituted compounds is related to the ability of aluminum to occupy manganese site and lithium site simultaneously, which force the valance state of manganese to decrease in order to balance the charge as shown from XPS results.

Fig. 9 shows a comparison of discharge capacity vs. number of cycles for all the cathode materials studied. Pristine Li_2MnO_3 initial discharge capacity was 12 mAh g^{-1} which was increasing for the first 25 cycles and eventually stabilized at a discharge capacity of ~24 mAh g^{-1}. The capacity behavior at the initial cycles is due to the cell formation in the coin cell and the capability of the electrolyte to get good contact with the electrode [30]. $Li_{0.5}Al_{0.5}MnO_3$ presents high capacity and good cycle stability compared to Al-substituted compounds and Li_2MnO_3. This improvement of the electrochemical performance is attributed to the insertion of aluminum ions into lithium and manganese sites simultaneously, which manage to decrease the valance state of manganese from 4+ to 3.5–3.8+. The cycle performance of $Li_{1.5}Al_{0.17}MnO_3$ and $Li_{1.0}Al_{0.33}MnO_3$ is presenting a slight disorder at the beginning of the charge/discharge
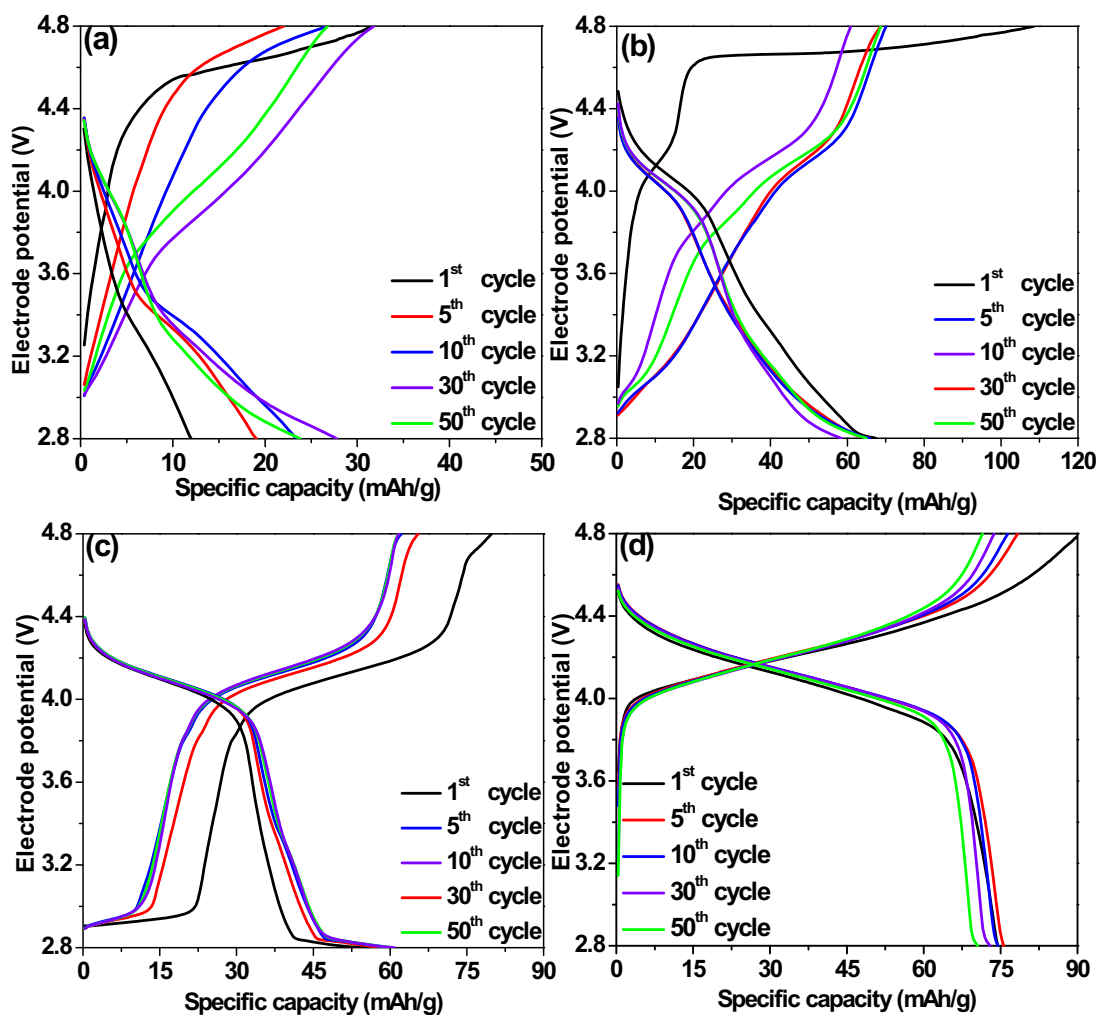
Fig. 8. Charge–discharge profiles of (a) Li_2MnO_3, (b) $Li_{1.5}Al_{0.17}MnO_3$, (c) $Li_{1.0}Al_{0.33}MnO_3$ and (d) $Li_{0.5}Al_{0.5}MnO_3$ using a current density of $10\,mAh\,g^{-1}$.

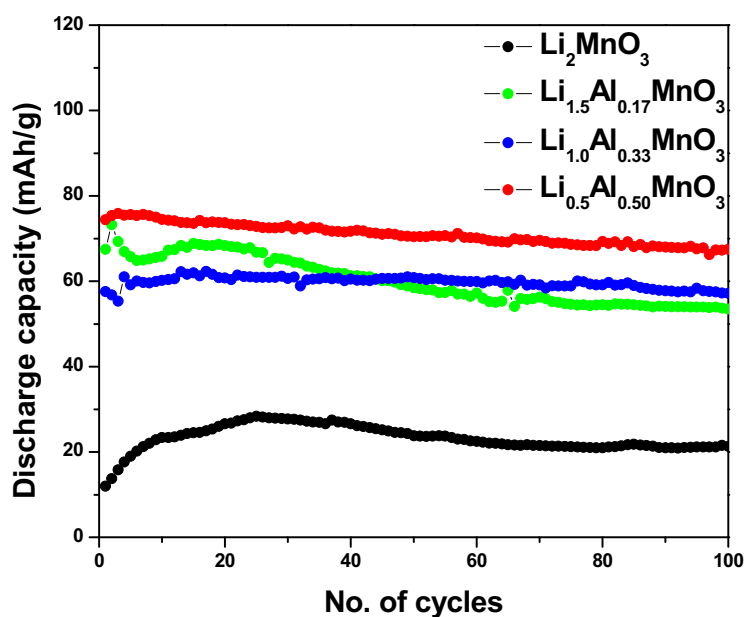**Fig. 9.** Comparison of the cycling performances for Li_2MnO_3 and Al-substituted compounds using a current density of $10\,mAh\,g^{-1}$ for 100 cycles.

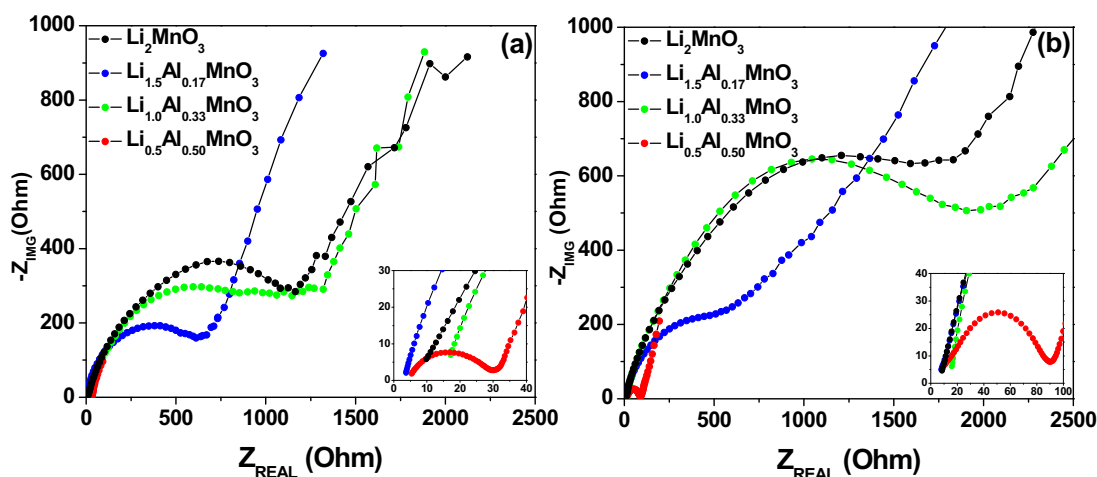**Fig. 10.** Nyquist plots of Li_2MnO_3, $Li_{1.5}Al_{0.17}MnO_3$, $Li_{1.0}Al_{0.33}MnO_3$ and $Li_{0.5}Al_{0.5}MnO_3$, (a) before cycling and (b) after three cycles.

Table 7
Electrochemical impedance spectroscopy (EIS): initial resistance (R_I) and charge transfer resistance (R_{CT}) before and after cycling.

Composition	R_I before (Ω)	R_I 3rd cycle (Ω)	R_{CT} before (Ω)	R_{CT} 3rd cycle (Ω)
Li_2MnO_3	26.77	8.44	1,164.13	1,831.10
$Li_{1.5}Al_{0.17}MnO_3$	17.14	15.86	1,316.08	2,093.51
$Li_{1.0}Al_{0.33}MnO_3$	3.65	7.77	603.07	478.68
$Li_{0.5}Al_{0.5}MnO_3$	5.34	10.54	30.14	89.55

analysis but stabilizes after the 15th cycle, indicating the best cycle stability for $Li_{1.0}Al_{0.33}MnO_3$ among the Al-substituted compounds.

Electrochemical impedance spectroscopy (EIS) measurements were performed on all the samples in order to monitor the cell resistance during charge/discharge cycles. The results for the pristine Li_2MnO_3 and Al -substituted materials are shown in Fig. 10 in the form of Nyquist plots. Fig. 10a shows the EIS measurements for the compounds before cycling. The initial resistance (R_I) of the coin cells and the charge transfer resistance (R_{CT}) are listed in Table 7. Li_2MnO_3 exhibited high initial resistance before cycling. However, the resistance decreased for consecutive cycles. A similar behavior was observed for $Li_{1.5}Al_{0.17}MnO_3$, where the initial resistance was high but decreased after cycling. The initial resistance for $Li_{0.5}Al_{0.5}MnO_3$ before cycling was $R_I = 5.34\,\Omega$ and increase to $R_I = 10.54\,\Omega$ after three cycles. The same phenomena occur for $Li_{1.0}Al_{0.33}MnO_3$, where the initial resistance increased after each cycle. In addition, we analyzed the charge transfer resistance for the compounds before cycling and after three cycles. The charge transfer resistance for the $Li_{0.5}Al_{0.5}MnO_3$ compound ($R_{CT} = 30.14\,\Omega$) is smaller than Li_2MnO_3 ($R_{CT} = 1164\,\Omega$), $Li_{1.0}Al_{0.33}MnO_3$ ($R_{CT} = 603\,\Omega$), and $Li_{1.5}Al_{0.17}MnO_3$ ($R_{CT} = 1316\,\Omega$), indicating that this composition facilitates electron transport at the interface between the electrode and the electrolyte compared to the others samples. Detailed EIS measurements are needed to understand the slow charge transfer at the electrode/electrolyte interface.

4. Conclusions

Li_2MnO_3, $Li_{1.5}Al_{0.17}MnO_3$, $Li_{1.0}Al_{0.33}MnO_3$ and $Li_{0.5}Al_{0.5}MnO_3$ were successfully synthesized by a sol–gel Pechini method. The compounds were characterized with XRD, where single phase was observed for the pristine Li_2MnO_3. The XRD profile for $Li_{1.5}Al_{0.17}MnO_3$, $Li_{1.0}Al_{0.33}MnO_3$ and $Li_{0.5}Al_{0.5}MnO_3$ indicated the presence of monoclinic/spinel phases, which was confirmed by Raman spectroscopy analysis and Neutron diffraction analysis. The spinel phase seems to form with increased aluminum substitution in the structure. X-ray photoelectron spectroscopy of Mn 2p

orbital showed a decrease in binding energy for $Li_{0.5}Al_{0.5}MnO_3$ and $Li_{1.0}Al_{0.33}MnO_3$, while the change in binding energy for $Li_{1.5}Al_{0.17}MnO_3$ was not significant. The shift to a lower binding energy for the samples indicates a decrease in the oxidation state of Mn, leading to a better electrochemical performance. These interpretations were supported by charge/discharge study at a current density of $10\,mA\,g^{-1}$, were an increase in capacity and better stability was observed for the $Li_{0.5}Al_{0.5}MnO_3$ ($70\,mA\,g^{-1}$) and $Li_{1.0}Al_{0.33}MnO_3$ ($62\,mA\,g^{-1}$) compounds.

References

[1] V. Etacheri, R. Marom, R. Elazari, G. Salitra, D. Aurbach, Energy Environ. Sci. 4 (2011) 3243–3262.
[2] J.B. Goodenough, K.-S. Park, J. Am. Chem. Soc. 135 (2013) 1167.
[3] H. Tao, Z. Feng, H. Liu, X. Kan, P. Chen, Open Mater. Sci. J. 5 (2011) 204–214.
[4] B.G. Pollet, I. Staffell, J.L. Shang, Electrochim. Acta 84 (2012) 235–249.
[5] J.H. Ryu, J. Eun, Y. Shin, Cathode Active Material Comprising Mixture of Lithium/Manganese Spinel Oxide and Lithium/Nickel/Cobalt/Manganese Oxide and Lithium Secondary Battery Containing Same, U.S. Patent and Trademark Office, Washington, DC, US Patent No. 7,816,033 B2 (2010).

[6] A.J. Paterson, A.R. Armstrong, P.G. Bruce, J. Electrochem. Soc. 151 (2004) A1552–A1558.
[7] R. Wang, X. He, L. He, F. Wang, R. Xiao, L. Gu, H. Li, L. Chen, Adv. Energy Mater. 3 (2013) 1358–1367.
[8] M.H. Rossouw, M.M. Thackeray, Mat. Res. Bull. 26 (1991) 463–473.
[9] S.H. Park, Y. Sato, J.K. Kim, Y.S. Lee, Mater. Chem. Phys. 102 (2007) 225–230.
[10] N. Tran, L. Croguennec, M. Menetrier, F. Weill, P. Biensan, C. Jordy, C. Delmas, Chem. Mater. 20 (2008) 4815–4825.
[11] M. Sathiya, K. Ramesha, G. Rousse, D. Foix, D. Gonbeau, A.S. Prakash, M.L. Doublet, K. Hemalatha, J.-M. Tarascon, Chem. Mater. 25 (2013) 1121–1131.
[12] D. Mori, H. Sakaebe, M. Shikano, H. Kojitani, K. Tatsumi, Y. Inaguma, J. Power Sources 196 (2011) 6934–6938.
[13] S. Kim, J.-K. Noh, S. Yu, W. Chang, J. Electroceram. 30 (2013) 159–165.
[14] S.F. Amalraj, D. Sharon, M. Talianker, C.M. Julien, L. Burlaka, R. Lavit, E. Zhecheva, B. Markovsky, E. Zinigrad, D. Kovacheva, R. Stoyanova, D. Aurbach, Electrochim. Acta 97 (2013) 259–270.
[15] F. Wang, S. Xiao, M. Li, X. Wang, Y. Zhu, Y. Wu, A. Shirakawa, J. Peng, J. Power Sources 287 (2015) 416–421.
[16] D. Xin, Y. Xu, L. Xiong, X. Sun, Z. Zhang, J. Power Sources 243 (2013) 78–87.
[17] M.P. Pechini, Method of Preparing Lead and Alkaline Earth Titanates and Niobates and Coating Method Using the Same to form a Capacitor, U.S. Patent and Trademark Office, Washington, DC, Us Patent 3,330,697 (1967).
[18] J.F. Moulder, W.F. Stickle, P.E. Sobol, K.D. Bomben, Handbook of X-ray Photoelectron Spectroscopy, Physical Electronics Inc, Eden Prairie, MN, 1982.
[19] N. Santander, S.R. Das, S.B. Majumder, R.S. Katiyar, Surf. Coat. Technol. 60 (2004) 177–178.
[20] P. Strobel, B. Lambert-Andron, J. Solid State Chem. 75 (1988) 90–98.
[21] T. Rao Penki, D. Shanmughasundaram, N. Munichandraiah, J. Solid State Electrochem. 17 (2013) 3125–3136.
[22] K. Kubobuchi, M. Mogi, H. Ikeno, I. Tanaka, H. Imai, T. Mizoguchi, Appl. Phys. Lett. 104 (2014) 053906.
[23] S.F. Amalraj, L. Burlaka, C.M. Julien, A. Mauger, D. Kovacheva, M. Talianker, B. Markovsky, D. Aurbach, Electrochem. Acta 123 (2014) 395–404.
[24] C. Julien, Solid State Ionics 136 (2000) 887–896.
[25] C. Julien, M. Massot, R. Baddour-Hadjean, S. Franger, S. Bach, J.P. Pereira-Ramos, Solid State Ionics 159 (2003) 345–356.
[26] D.Y.W. Yu, K. Yanagida, J. Electrochem. Soc. 158 (9) (2001) A1015–A1022.
[27] J. Preudhomme, P. Tarte, Spectrochim. Acta 27A (1971) 845–851.
[28] D.Y.W. Yu, K. Yanagida, Y. Kato, H. Nakamura, J. Electrochem. Soc. 156 (6) (2009) A417–A424.
[29] S.F. Amalraj, B. Markovsky, D. Sharon, M. Talianker, E. Zinigrad, R. Persky, O. Haik, J. Grinblat, J. Lampert, M. Schulz-Dobrick, A. Garsuch, L. Burlaka, D. Aurbach, Electrochim. Acta 78 (2012) 32–39.
[30] J. Gim, J. Song, H. Park, J. Kang, K. Kim, V. Mathew, J. Kim, Nanoscale Res. Lett. 7 (60) (2012) 1–9.